

Fuse4Seg: Image-Level Fusion Based Multi-Modality Medical Image Segmentation

Yuchen Guo^{1*}, Weifeng Su^{1,2†}

¹Beijing Normal University - Hong Kong Baptist University United International College

²Guangdong Provincial Key Laboratory of Interdisciplinary Research and Application for Data Science
r130026037@mail.uic.edu.hk, wfsu@uic.edu.cn

Abstract

Although multi-modality medical image segmentation holds significant potential for enhancing the diagnosis and understanding of complex diseases by integrating diverse imaging modalities, existing methods predominantly rely on feature-level fusion strategies. We argue the current feature-level fusion strategy is prone to semantic inconsistencies and misalignments across various imaging modalities because it merges features at intermediate layers in a neural network without evaluative control. To mitigate this, we introduce a novel image-level fusion based multi-modality medical image segmentation method, *Fuse4Seg*, which is a bi-level learning framework designed to model the intertwined dependencies between medical image segmentation and medical image fusion. The image-level fusion process is seamlessly employed to guide and enhance the segmentation results through a layered optimization approach. Besides, the knowledge gained from the segmentation module can effectively enhance the fusion module. This ensures that the resultant fused image is a coherent representation that accurately amalgamates information from all modalities. Moreover, we construct a *BraTS-Fuse* benchmark based on BraTS dataset, which includes 2040 paired original images, multi-modal fusion images, and ground truth. This benchmark not only serves image-level medical segmentation but is also the largest dataset for medical image fusion to date. Extensive experiments on several public datasets and our benchmark demonstrate the superiority of our approach over prior state-of-the-art (SOTA) methodologies.

Introduction

In medical imaging, segmentation is a critical task that involves identifying and delineating anatomical structures or pathological regions within images (Chen et al. 2022; Isensee et al. 2018; Ibtehaz and Kihara 2023). Traditional single-modality approaches often fall short in providing comprehensive insights, as each imaging modality has its own strengths and limitations (Lou, Guan, and Loew 2021; Huang et al. 2020). Recent research has increasingly focused on the handling of multimodal information. In the domain of medical image analysis, **Multi-Modality Medical Image**

Segmentation (MM-MIS) represents a prominent research direction. MM-MIS is dedicated to exploiting the complementary information afforded by various imaging modalities, *e.g.* Magnetic Resonance Imaging (MRI), Computed Tomography (CT), Positron Emission Tomography (PET) and *etc.*, to enhance the precision and robustness of medical image segmentation.

Among the various imaging techniques, Multi-Modality MRI has gained considerable attention due to its ability to capture different aspects of tissue characteristics, *i.e.*, T1, T1ce, T2-weighted MRI, and FLAIR MRI images each provide unique information about tissue structures and abnormalities. T1-weighted images are particularly useful for visualizing anatomical details and identifying structural abnormalities, while T2-weighted images enhance the visibility of lesions and edema. FLAIR MRI, on the other hand, is especially effective in detecting abnormalities in areas close to cerebrospinal fluid.

The integration of multimodal MRI images seeks to harness the strengths of each modality to enhance the accuracy of segmentation tasks. Existing approaches often rely on feature-level fusion strategies (Chen et al. 2017, 2018), which aggregate in the intermediate layers of the segmentation architecture, as illustrated in Fig. 1 (right). These methods extract features in the initial stages of the entire segmentation architecture and then combine different feature maps through simple concatenation or element-wise aggregation operations before obtaining the final fused embedding through a decoder. While these approaches may preliminarily merge modality-specific pathological information, they are prone to semantic inconsistencies and misalignments across different modalities. This leads to a “black box” scenario, where the intermediate fusion processes and their effects on segmentation outcomes remain inadequately understood. Despite achieving promising visual results and leading performance metrics in segmentation tasks, the lack of effective evaluation and interpretability of the fusion process remains a significant challenge, known as the semantic inconsistencies and misalignments problem (Lu et al. 2016; Atrey, Singh, and Bodhey 2024).

On the other hand, current image fusion methods mainly focus on situations in general environments based on infrared image and visible image (IVIF), while the technology for multimodal fusion of medical images (MIF) remains in

*Part of this research was performed during Yuchen Guo’s internship at MMLab@SIAT, CAS.

†Corresponding author.

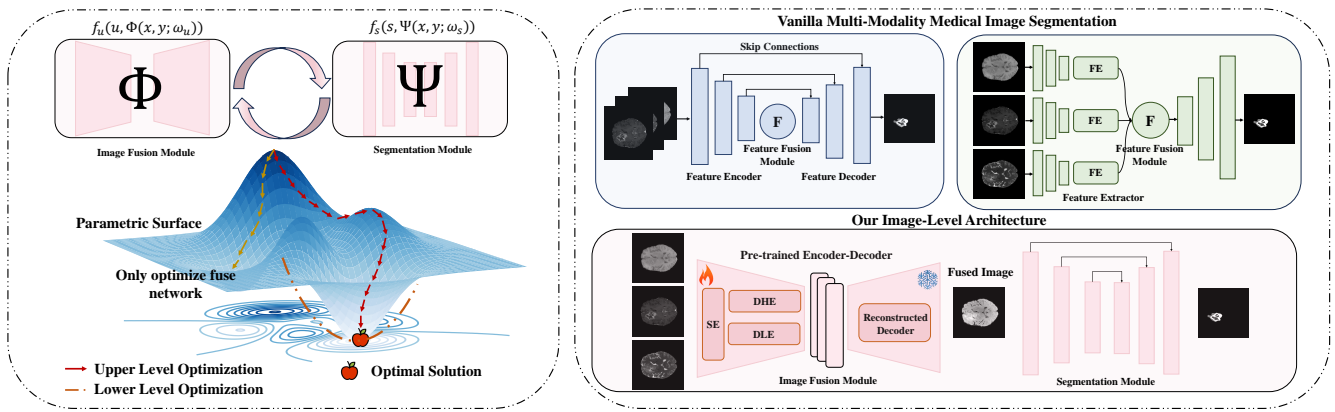


Figure 1: (left) The bi-level optimization learning process with fusion task as the leader and segmentation task as follower. (right) Existing Multi-Modality Medical Image Segmentation Methods vs. Our Fuse4Seg. The DHE and DLE are donotes to Deep High-frequency Encoder and Deep Low-frequency Encoder, respectively.

its nascent stages. Existing MIF primarily emphasizes improving the visual quality of fused images and optimizing evaluation metrics for these images, without addressing the development of suitable medical downstream tasks.

To mitigate these challenges, we present a novel image-level fusion based multi-modality medical image segmentation approach, *Fuse4Seg*. It is a bi-level learning framework designed to model the intertwined dependencies between medical image segmentation and medical image fusion, with the ultimate aim of guiding a bi-level optimization formulation for the joint problem towards a stable optimum. Fuse4Seg is comprised of two modules involving fusion network and segmentation network.

During the pre-training stage, we introduce two discriminative blocks into a correlation driven encoder in the fusion module. The purpose of these discriminative block is to guide the feature decomposition and extraction capabilities of encoder throughout the reconstructive process. In the main training stage, a cooperative training strategy is employed to learn the optimal parameters for both the fusion and segmentation modules. As illustrated in Fig. 1 (left), the image fusion task is assigned as the upper-level problem, while the image segmentation task is designated as the lower-level problem. This hierarchical structure allows the fusion process to guide and enhance the segmentation results through a layered optimization approach.

By fusing at the image level, our approach inherently maintains the semantic integrity of the input data. This ensures that the resultant fused image is a coherent representation that accurately amalgamates information from all modalities. The dual network structure further fine-tunes both the fusion and segmentation processes in unison, leading to more precise and reliable segmentation outcomes. The bi-level optimization guarantees that the fusion process is tailored to maximize the utility of the resulting image for subsequent segmentation tasks. This underscores the critical role of image-level fusion in enhancing the overall effectiveness of the system. Our contributions can be summarized as four aspects:

- We first propose an image-level fusion guided multi-modality medical image segmentation framework, termed *Fuse4Seg*. Extensive experiments conducted on several public datasets and our benchmark demonstrate that our method boost the performance compared to state-of-the-art (SOTA) approaches.
- We design a joint fusion-segmentation network utilizing a bi-level optimization learning formulation, which simultaneously addresses both tasks, producing not only superior fusion results but also enhanced segmentation performance.
- We introduce a two training scheme from the bi-level formulation yielding optimal network parameters, which includes a pre-train stage and a cooperative training stage with newly designed loss function to enhance the overall performance and convergence of the network.
- We build a brain tumor fusion image dataset specifically for medical segmentation (*BraTS-Fuse*) based on BraTS2021, which contains 2,040 aligned cases. Each case includes different T1 modality images, T1ce modality images, T2 modality images, FLAIR modality images, a segmented ground truth, and a series of cross-fused images.

Related Works

Medical Image Segmentation

Medical image segmentation, a critical task involving pixel-wise classification of anatomical structures across imaging modalities like MRI and CT, has seen substantial advancements with U-shaped networks (Chen et al. 2022; Isensee et al. 2018; Ibtihaz and Kihara 2023; Lou, Guan, and Loew 2021; Huang et al. 2020). Other notable developments include DeepLab series (Chen et al. 2017, 2018), which employed atrous convolutions and spatial pyramid pooling for effective multi-scale information processing. Moreover, TransUNet (Chen et al. 2021) combining CNNs for local feature extraction with transformers for global context modeling, and Swin-Unet (Cao et al. 2022) incorporating Swin

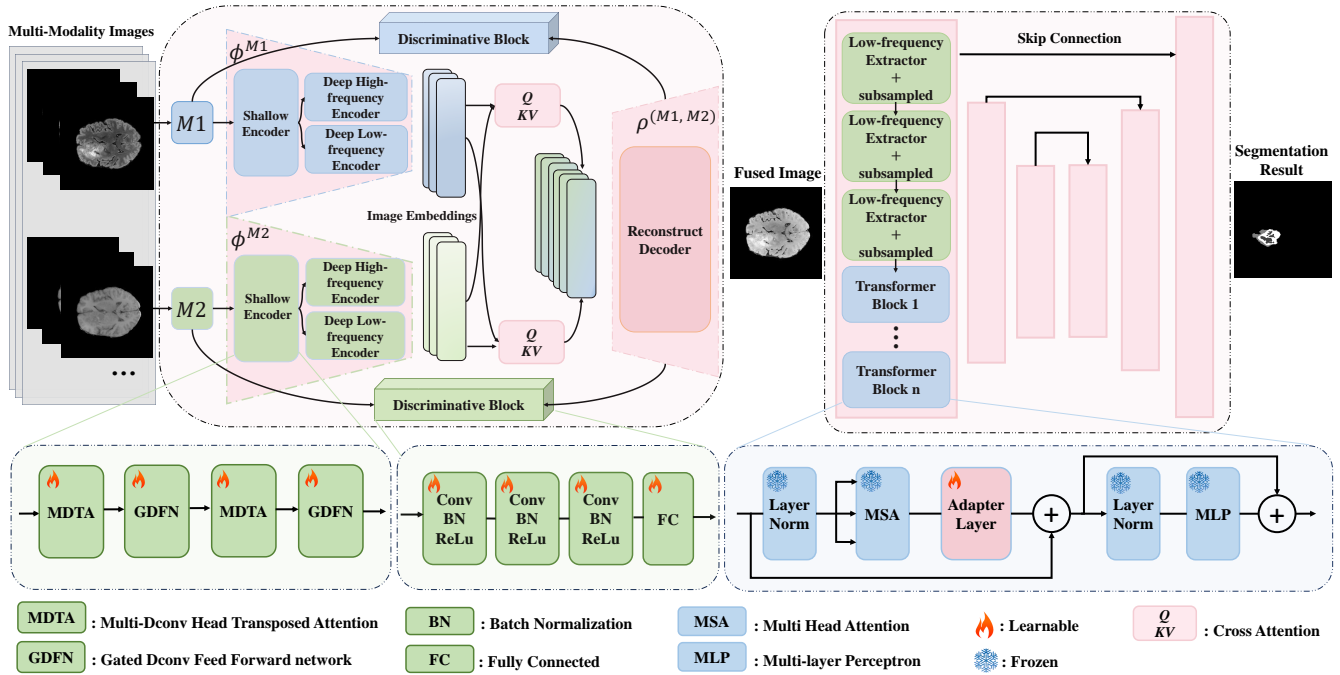


Figure 2: The overall framework of our Fuse4Seg, which consist of a fusion module and a segmentation module.

Transformer blocks within a U-shaped architecture. However, these methods predominantly focus on feature-level fusion, thereby neglecting the significance of the holistic image.

Image Fusion

Current image fusion research predominantly targets infrared and visible image fusion (IVIF), with limited focus on medical images (MIF). Existing multi-modality image fusion methods can be categorized into two main groups: generative models (Ma et al. 2019, 2020a,b) and autoencoder-based models (Li and Wu 2018; Li, Wu, and Kittler 2021a; Zhang and Ma 2021). Generative models use GANs (Ma et al. 2019, 2020a,b) or denoising diffusion models (Zhao et al. 2023b) to represent the latent space distribution of fused and source images. Autoencoder-based models employ encoder/decoder structures with CNNs or Transformers. Moreover, for the natural images, multi-modality image fusion is often part of coupled systems, incorporating downstream tasks like object detection and segmentation (Liu et al. 2023, 2022; Sun et al. 2022; Tang, Yuan, and Ma 2022). Our work successfully bridge this gap in MIF.

Methodology

In this section, we present the formulation of our bi-level optimization framework, followed by the solution process and corresponding cooperative training strategy employed. We then introduce our joint fusion-segmentation network, detailing the loss functions for each components.

Bi-level Optimization

Initially, the medical image fusion (MIF) considered as a preliminary task for the joint cross-modality features based medical iamge segmentation (MIS). This method aims to bridge the gap between medical image fusion and segmentation, which named image-level fusion guided segmentation, enhanced visual quality and improved semantic understanding, benefiting subsequent analytical tasks. We assume that both images with different modalities, $M1$ and $M2$, are of size $m \times n$ and represented as column vectors \mathbf{x} , \mathbf{y} . Additionally, we use $\theta \in \mathbb{R}^{mn \times 1}$ for representation to the fused result.

In this paper, bi-level optimization problem is modeled using Stackelberg game theory (Colson, Marcotte, and Savard 2007; Ochs et al. 2015), where the fusion module plays the role of leader (upper-level task) and the segmentation acts as the follower (lower-level task). Different to other methods, We first introduce the framework in which the medical segmentation module uses the fused image generated by the fusion module as input. This structure naturally captures the sequential nature of our task, as fusion precedes segmentation, and allows us to optimize both tasks simultaneously while maintaining their individual objectives. Meanwhile, by taking the fusion strategy on image dimension, our approach avoids the problem including misalignment and semantic displacement because the pixel is matched scale for the inputs and corresponding output. Moreover, Stackelberg game theory provides a mathematical framework for optimization process handling the interdependence between fusion and segmentation. Initially, supposing the fusion process can be donated as \mathcal{F} , and let

$\theta = \mathcal{F}(M1, M2)$ formally, so the bi-level optimization problem is expressed as:

$$\begin{aligned} & \min_{\omega_s} \mathcal{L}^s(\Psi(\theta^*; \omega_s)), \\ & \text{s.t. } \theta^* \in \arg \min_{\theta} f(\theta; \mathbf{x}, \mathbf{y}) + g_{M1}(\theta; \mathbf{x}) + g_{M2}(\theta; \mathbf{y}), \end{aligned} \quad (1)$$

where ω_s denotes the parameters of the segmentation network, Ψ represents the segmentation network, $g_{M1}(\cdot)$ and $g_{M2}(\cdot)$ are constraints for the two modalities, and $f(\cdot)$ is a fidelity term.

To achieve visually appealing fused images and accurate scene segmentation results, we jointly formulate the two tasks as:

$$\min_{\omega_s, \omega_f} \mathcal{L}^s(\Psi(\theta^*; \omega_s)), \text{ s.t. } \theta^* = \Phi(\mathbf{x}, \mathbf{y}; \omega_f), \quad (2)$$

where Φ represents the medical image fusion network ($f_{\theta}(\theta, \Psi(x, y; \omega_f))$) and Ψ represents the segmentation network ($f_s(s, \Psi(x, y; \omega_s))$). A visual illustration is provided in Fig. 1 (left).

Training Strategy

Training the joint fusion and segmentation networks involves solving the bi-level optimization problem with respect to $\omega = \{\omega_s, \omega_f\}$. Follow the (Fan et al. 2024), We develop a numerical solution starting from the upper-level objective, computing its gradient with respect to ω_s :

$$\begin{aligned} \nabla_{\omega_s} \mathcal{L}^s(\Psi(\theta^*; \omega_s)) &= \nabla_{\omega_s} \mathcal{L}^s(\Psi(\theta; \omega_s)) \\ &+ \nabla_{\theta} \mathcal{L}^s(\Psi(\theta; \omega_s)) \nabla_{\omega_s} \theta^* \end{aligned} \quad (3)$$

where the first term is the direct gradient with respect to ω_s , and the second term accounts for the latent connection with the fusion network.

To efficiently compute gradients, we use the Gauss-Newton approximation, which simplifies the problem to first-order computations. The gradient response θ^* is expressed as:

$$\nabla_{\theta} \mathcal{L}^s = \nabla_{\theta} \mathcal{L}^s(\Psi(\theta^*(\omega_s); \omega_s)) \nabla_{\omega_s} \theta^*. \quad (4)$$

Using the implicit function theorem, we avoid computationally expensive nested optimization loops. By setting $\partial \mathcal{L}^f / \partial \omega_f = 0$, we obtain the gradient of θ^* with respect to ω_s as follows:

$$\nabla_{\omega_s} \theta^*(\omega_s) = - [\nabla_{\theta\theta}^2 \mathcal{L}^f(\Phi(\mathbf{x}, \mathbf{y}; \omega_f))]^{-1} \cdot \mathcal{W}_{Hes}, \quad (5)$$

where $\nabla_{\theta\theta}^2$ denotes the second-order partial derivatives of the fusion loss function \mathcal{L}^f with respect to θ , and $\mathcal{W}_{Hes} = \nabla_{\theta, \omega_s}^2 \mathcal{L}^f(\theta, \omega_s)$ represents the cross-gradient term. This expression involves the inversion of the second-order derivatives and the Hessian matrix.

Then, we introduce the new fusion regularity term \mathcal{L}^f into the total loss function and use it as a weighting term for detecting losses:

$$\begin{aligned} & \min_{\omega_s, \omega_f} \mathcal{L}^s(\Psi(\theta^*; \omega_s)) + \lambda \mathcal{L}^f(\Phi(\mathbf{x}, \mathbf{y}; \omega_f)), \\ & \text{s.t. } \theta^* = \Phi(\mathbf{x}, \mathbf{y}; \omega_f), \end{aligned} \quad (6)$$

where loss gradients with respect both ω_s, ω_f can be calculated as:

$$\frac{\partial \mathcal{L}^s}{\partial \omega_s} = \frac{\partial \mathcal{L}^s}{\partial \Psi_s} \frac{\partial \Psi_s}{\partial \omega_s}, \quad \frac{\partial \mathcal{L}^s}{\partial \omega_f} = \frac{\partial \mathcal{L}^s}{\partial \Psi_s} \frac{\partial \Psi_s}{\partial \Psi_f} \frac{\partial \Psi_f}{\partial \omega_f} + \lambda \frac{\partial \mathcal{L}^f}{\partial \Psi_f} \frac{\partial \Psi_f}{\partial \omega_f}. \quad (7)$$

Fusion module

Pre-trained Decomposition Encoder Initially, we introduce the correlation coefficient guided pre-trained dual stream encoder. As discussed in (Si et al. 2022; Li et al. 2022), Convolutional Neural Network (CNN) based models are proficient at capturing high-frequency local information, whereas Transformer-based models are primarily oriented towards processing low-frequency global features. We adopt Lite Transformer (Wu et al. 2020) blocks leveraging longrange attention to handle low-frequency global features and Invertible Neural Networks blocks focusing on extracting high-frequency local information. This architecture is inspired by (Ardizzone et al. 2018), we redesign it through a large-scale medical image dataset using extensive image pairs.

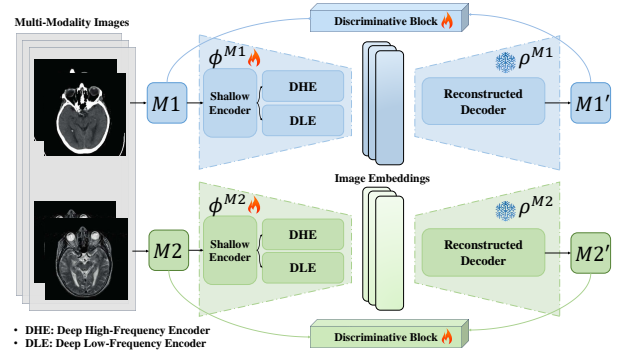


Figure 3: The diagram illustrates the architecture of a pre-trained dual-stream decomposition encoder.

Image Level Fusion Network The image-level fusion network leverages a pre-trained encoder to extract both modality-specific and modality-shared features. Then the same frequency features from different modalities fused respectively, then combined by cross-attention. As shown in Fig. 2, after extracting features from encoders ($\Phi(M1)$, $\Phi(M2)$), embeddings of images from two modalities are obtained. Here we use the embedding of $M1$ as the Query Q , while the embeddings of $M2$ as the Key K and the Value V . Assuming the attention guided embeddings are denoted as: ($\Phi(\hat{M}1)$) and ($\Phi(\hat{M}2)$). The mapping can be expressed as:

$$\begin{aligned} & \text{CroAttn}_{\Phi(M1) \rightarrow \Phi(M2)}(\Phi(M1), \Phi(M2)) \\ &= \text{softmax} \left(\frac{(\mathbf{W}_q \Phi(M1) \Phi(M2)^T \mathbf{W}_k^T)}{\sqrt{d_k}} \right) \mathbf{W}_v \Phi(M2) \\ &\rightarrow A_{\text{croattn}} \mathbf{W}_v(\Phi(M2)) \rightarrow (\Phi(\hat{M}2)) \end{aligned} \quad (8)$$

where \mathbf{W}_q , \mathbf{W}_v and \mathbf{W}_k are trainable weight matrices multiplied to queries ($Q_{\Phi(M1)}$) and key-value pair ($K_{\Phi(M2)}$),

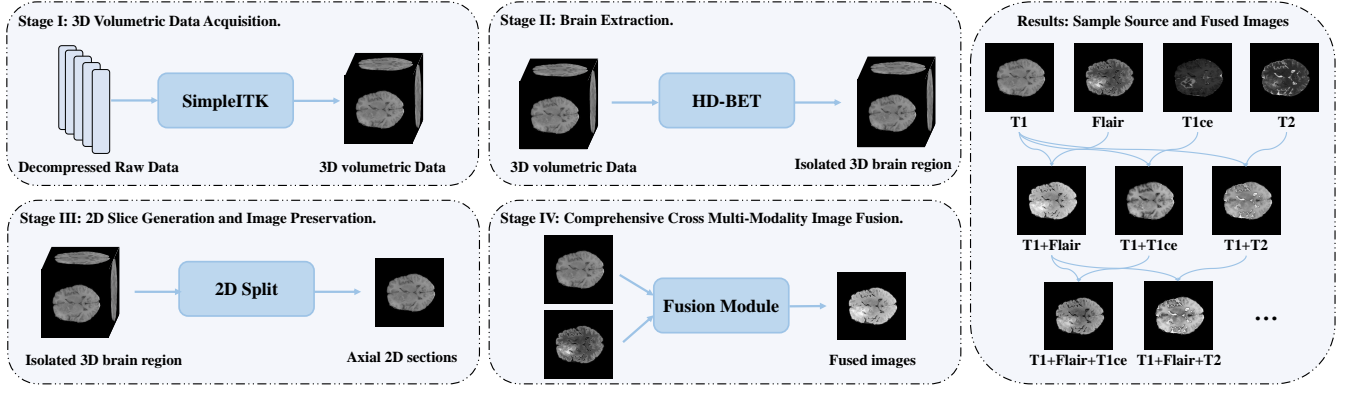


Figure 4: The data processing pipeline of our BraTS-Fuse dataset and samples of both source images and fused images. As a reference, our dataset, which built upon the BraTS2021 dataset, contains 2,040 aligned cases.

$V_{\Phi(M_2)}$), and A_{croattn} is the cross-attention matrix for computing the weighted average of $\Phi(M_2)$.

Furthermore, the attention maps generated during this process are utilized to highlight semantic information within the fused image. These maps provide a clear visualization of the regions where important features from each modality are being integrated, helping to ensure that critical semantic content is preserved during fusion. This approach allows the model to focus on the most relevant parts of each image, thereby enhancing the semantic coherence of the final output. Additionally, the attention maps offer insights into the contribution of each modality at a more granular level.

Segmentation module

In the segmentation module, we continue to employ a CNN-Transformer architecture to maintain coherence with the fusion module. However, we adopt a hybrid approach that integrates the Transformer within the CNN framework as our backbone in TransUNet, and we combine each small block in a manner resembling the MedSAM2d architecture within the segmentation module. By leveraging the strengths of both convolutional operations and attention mechanisms, this hybrid framework significantly enhances segmentation performance. As introduced in (Cheng et al. 2023), A skip connection is added after each adapter layer. More detail statements are shown in supplementary materials.

Loss Function

In this section, we will first introduce the loss function for the image fusion module and the corresponding pre-training stage, followed by a discussion of the loss function for the segmentation module.

Loss Function for Pre-Training Stage The loss function for pre-training decomposition encoder is divided into two parts: adversarial loss and content loss:

$$\mathcal{L}_{Enc} = \lambda \mathcal{L}_{Enc}^{adv} + \sigma \mathcal{L}_{Enc}^{correlation} + (1 - \sigma) \mathcal{L}_{Enc}^{content} \quad (9)$$

where σ and λ are hyper-parameters controlling the trade-off between these terms.

We design the adversarial game between image before/after reconstruction for pre-training. The adversarial loss for the encoder can be written as:

$$\mathcal{L}_{Enc}^{adv} = \mathbb{E} \left[\log \left(1 - D_{M_1}(\tilde{M}_1) \right) \right] + \mathbb{E} \left[\log \left(1 - D_{M_2}(\tilde{M}_2) \right) \right] \quad (10)$$

Additionally, we use correlation decomposition loss (Zhao et al. 2023a) to differentiate high-frequency features from low-frequency features:

$$\mathcal{L}_{Enc}^{correlation} = \frac{CC(\phi_{DH}(M_1), \phi_{DH}(M_2))^2}{CC(\phi_{DL}(M_1), \phi_{DL}(M_2)) + \epsilon} \quad (11)$$

where ϵ is set to 1.01 to ensure the result is always positive.

In the pre-train stage, we introduce the content loss function consists of the square of the L_2 norm and structural similarity index:

$$\mathcal{L}_{Dec}^{content} = \|M_1 - D(M_1)\|_2^2 + (1 - \text{SSIM}(M_1, D(M_1))) \quad (12)$$

Loss Function for Fusion Module In this training stage, the inputs of the discriminative blocks have changed to fused image and two source images, respectively. we represent the adversarial loss in Eq. 10 where the input becomes $\theta = \mathcal{F}(M_1, M_2)$. Similarly, the content loss for this stage changed as:

$$\mathcal{L}_{text} = \frac{1}{HW} \|\nabla I_f - \max(|\nabla M_1|, |\nabla M_2|)\|_1 \quad (13)$$

Loss function for segmentation module The segmentation module only trained in the cooperative training stage, and the entire loss function can be divided into a cross-entropy loss and a dice loss, which are written as:

$$\mathcal{L} = \alpha \mathcal{L}_{CE} + \beta \mathcal{L}_{Dice}. \quad (14)$$

Benchmark

In multi-modality medical image segmentation (MIS), most existing datasets predominantly contain source images and

Table 1: Quantitative comparisons on BraTS-Fuse datasets for MIF and MIS. Bold red indicates the best, and bold blue indicates the second best. First row present the fusion comparisons and second row present segmentation results.

Dataset: T1-T2 Fusion								Dataset: T1-T1ce Fusion								Dataset: T1-FLAIR Fusion							
EN	SD	SF	MI	SCD	VIF	Qabf		EN	SD	SF	MI	SCD	VIF	Qabf		EN	SD	SF	MI	SCD	VIF	Qabf	
DID	4.37	58.34	34.64	1.71	0.69	0.41	0.38	DID	3.97	65.12	24.62	1.63	0.42	0.41	0.53	DID	2.97	55.12	13.69	1.51	0.42	0.46	0.51
U2F	4.21	61.98	32.54	2.08	0.75	0.37	0.46	U2F	3.83	59.66	24.58	1.61	0.44	0.32	0.43	U2F	3.45	45.66	14.58	1.54	0.44	0.36	0.45
RFN	4.97	70.36	33.42	1.98	0.68	0.43	0.52	RFN	3.84	64.50	25.51	1.77	0.39	0.52	0.62	RFN	3.53	44.50	16.51	1.89	0.39	0.51	0.62
DDc	4.26	62.56	30.61	1.72	0.65	0.38	0.42	DDc	3.78	66.33	23.48	1.72	0.35	0.36	0.47	DDc	3.33	49.33	13.48	1.72	0.35	0.46	0.36
Tar	4.35	61.14	28.38	1.94	0.92	0.32	0.56	Tar	4.02	65.63	23.54	1.62	0.32	0.46	0.54	Tar	3.02	65.63	15.54	1.62	0.32	0.48	0.58
CDD	4.49	71.36	34.02	2.16	1.18	0.44	0.56	CDDF	4.02	74.15	25.48	1.78	1.42	0.57	0.65	CDD	3.67	52.68	17.32	1.83	0.96	0.58	0.64
DDF	4.77	69.35	32.77	1.98	1.03	0.41	0.54	DDF	4.06	71.42	25.69	1.66	0.49	0.54	0.71	DDF	3.57	56.42	16.81	1.66	0.49	0.53	0.55
Ours	4.83	76.19	35.56	2.2	1.21	0.49	0.57	Ours	4.45	75.11	29.2	1.87	1.68	0.66	0.65	Ours	4.17	62.61	22.56	1.87	1.58	0.68	0.70

Dataset: T1-T2 Segmentation				Dataset: T1-T1ce Segmentation				Dataset: T1-FLAIR Segmentation			
	Dice(%)	mIoU	HD95↓		Dice(%)	mIoU	HD95↓		Dice(%)	mIoU	HD95↓
UNet 3+	85.23	79.12	6.84	UNet 3+	88.14	81.76	5.45	UNet 3+	86.92	80.34	5.87
AttnUNet	87.56	81.34	5.67	AttnUNet	89.67	83.32	4.98	AttnUNet	88.45	82.12	5.35
SwinUNet	84.76	82.07	5.42	SwinUNet	89.33	84.02	4.72	SwinUNet	88.50	82.60	5.14
CASCADE	86.45	80.21	6.12	CASCADE	88.76	82.45	5.21	CASCADE	87.56	81.02	5.61
EMCAD	87.12	78.64	7.03	EMCAD	88.34	80.67	5.78	EMCAD	86.13	79.68	6.02
FILM+nnUNet	88.05	82.36	5.31	FILM+nnUNet	89.98	83.90	4.61	FILM+nnUNet	88.92	82.70	5.03
FILM+nnUNet-p	88.32	81.02	5.58	FILM+nnUNet-p	90.00	83.50	4.85	FILM+nnUNet-p	89.02	82.84	5.27
Ours	89.24	83.45	4.97	Ours	90.85	85.23	4.48	Ours	89.78	84.12	4.89

their corresponding segmentation ground truths. However, the introduction of a new segmentation framework that leverages fused images necessitates the creation of a robust benchmark. In this study, we employ brain MR images as a quintessential example of MIS due to their widespread application in both clinical practice and research. Brain MR images, encompassing modalities such as T1, T2, and FLAIR, provide a wealth of complementary information crucial for precise segmentation. For instance, T1-weighted images offer intricate details of the anatomical structure, T2-weighted images emphasize fluid and pathological alterations, while FLAIR images excel in lesion visualization. Our goal is to assemble a comprehensive multi-modality fusion baseline image dataset, comprising images fused from 2, 3, and 4 modalities. This foundational fusion dataset serves as a springboard for future research, enabling further exploration and enhancement of medical image segmentation quality by utilizing fused images as inputs within innovative architectural frameworks for segmentation models.

On the other hand, the only widely-used existing medical image fusion dataset is the Harvard¹ dataset, which contains approximately 300 paired images. Although valuable for various studies, it falls short of meeting the demands of current advanced models, highlighting a significant data scarcity issue that challenges researchers aiming to improve rigorous and comprehensive models accuracy and robustness. Our dataset, which contains 2,040 paired case images, addresses this critical gap by providing a more extensive and

diverse collection of medical images.

Data Processing

To obtain high-quality image level fusion based medical image segmentation source pairs, we adopt the following four stages to process the raw data. Fig. x illustrate our data processing pipeline and samples.

Stage I: 3D Volumetric Data Acquisition. Employ the state-of-the-art medical imaging library SimpleITK² to load the decompressed 3D data. This process results in a three-dimensional array containing the volumetric data, where each element corresponds to a voxel.

Stage II: Brain Extraction. Utilize advanced brain extraction tools HD-BET(Isensee et al. 2019) to process the 3D data and isolate the brain region. This step effectively removes non-brain tissues, ensuring that subsequent processing is concentrated solely on the brain tissue.

Stage III: 2D Slice Generation and Image Preservation. Extract 2D slices from the processed 3D data, selecting the slice orientation based on specific requirements, such as axial cross-sections. Each slice is saved as an individual ‘.png’ image file, ensuring that the resolution and image quality meet the required standards.

Stage IV: Comprehensive Cross Multi-Modality Image Fusion. Apply our fusion model to generate fused images from combinations of two, three, and four modalities. This

¹<http://www.med.harvard.edu/AANLIB/home.html>

²<https://simpleitk.org/>

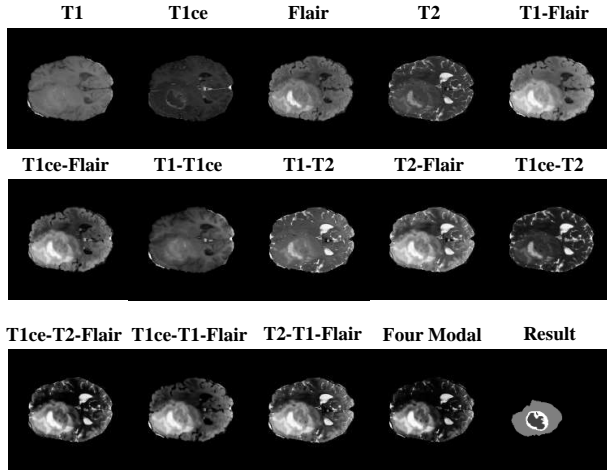


Figure 5: The fusion and segmentation results.

stage integrates information across multiple modalities to produce comprehensive fusion images. The specific fusion metrics, along with comparative experiments, are presented in next section.

Experiments

We not only evaluate our model on Medical Image Segmentation (MIS) tasks but also conduct comparative experiments with other Medical Image Fusion (MIF) models for our fused images. To demonstrate the applicability of our approach in both MIS and MIF, we utilize training data from the *BraTS-Fusion* dataset that we built. Additionally, to ensure a fair comparison with state-of-the-art MIF methods, we adhere to the same test set used in previous work, following the official train/test split for the Harvard evaluation. Furthermore, we compare the performance of other MIS state-of-the-art methods on the BraTS2021 dataset. Our experiments were implemented based on the PyTorch framework and performed on a NVIDIA A100 GPU.

Setup

For the pre-trained encoder, we trained 80 epochs for both the encoder-decoder and discriminative block, while in the fusion phase, the model was trained with 140 epochs. We use the Adam optimizer for the encoder-decoder and the discriminative block, with an initial learning rate of $1e-4$, which decreases by a factor of 0.5 every 20 epochs. The training samples are randomly cropped into 224×224 patches in preprocessing stage and the batch size is set to 16. The segmentation module is trained using the SGD optimizer with a learning rate of 0.01, momentum of 0.9, and weight decay of $1e-4$.

Visualization of medical image fusion

In this section, we first evaluate the image fusion results with the state-of-the-art methods including DIDFuse (Zhao et al. 2020), U2Fusion (Xu et al. 2020), RFN-Nest (Li, Wu, and Kittler 2021b), DDcGAN (Ma et al. 2020c), TarDAL (Liu

Table 2: Quantitative comparisons on MRI-CT, MRI-PET, and MRI-SPECT datasets. Bold red indicates the best, and bold blue indicates the second best, respectively.

Dataset: MRI-CT							
	EN	SD	SF	MI	SCD	VIF	Qabf
DIDFuse	4.37	58.34	34.64	1.71	0.69	0.41	0.38
U2Fusion	4.21	61.98	32.54	2.08	0.75	0.37	0.46
RFN-Nest	4.97	70.36	33.42	1.98	0.68	0.43	0.52
DDcGAN	4.26	62.56	30.61	1.72	0.65	0.38	0.42
TarDAL	4.35	61.14	28.38	1.94	0.92	0.32	0.56
CDDFuse	4.49	71.36	34.02	2.16	1.18	0.44	0.56
DDFM	4.77	69.35	32.77	1.98	1.03	0.41	0.54
Ours	4.83	76.19	35.56	2.2	1.21	0.49	0.57
Dataset: MRI-PET							
	EN	SD	SF	MI	SCD	VIF	Qabf
DIDFuse	3.97	65.12	24.62	1.63	0.42	0.41	0.53
U2Fusion	3.83	59.66	24.58	1.61	0.44	0.32	0.43
RFN-Nest	3.84	64.50	25.51	1.77	0.39	0.52	0.62
DDcGAN	3.78	66.33	23.48	1.72	0.35	0.36	0.47
TarDAL	4.02	65.63	23.54	1.62	0.32	0.46	0.54
CDDFuse	4.02	74.15	25.48	1.78	1.42	0.57	0.65
DDFM	4.06	71.42	25.69	1.66	0.49	0.54	0.71
Ours	4.45	75.11	29.2	1.87	1.68	0.66	0.65
Dataset: MRI-SPECT							
	EN	SD	SF	MI	SCD	VIF	Qabf
DIDFuse	2.97	55.12	13.69	1.51	0.42	0.46	0.51
U2Fusion	3.45	45.66	14.58	1.54	0.44	0.36	0.45
RFN-Nest	3.53	44.50	16.51	1.89	0.39	0.51	0.62
DDcGAN	3.33	49.33	13.48	1.72	0.35	0.46	0.36
TarDAL	3.02	65.63	15.54	1.62	0.32	0.48	0.58
CDDFuse	3.67	52.68	17.32	1.83	0.96	0.58	0.64
DDFM	3.57	56.42	16.81	1.66	0.49	0.53	0.55
Ours	4.17	62.61	22.56	1.87	1.58	0.68	0.70

et al. 2022), CDDFuse (Zhao et al. 2023a) and DDFM (Zhao et al. 2023c).

Qualitative Comparisons The qualitative results of our method and other competitive approaches are shown in Fig. 6, using an MRI-CT fusion example from the Harvard dataset.

Quantitative Comparisons There are usually eight unsupervised metrics to measure the quantitative performance of MIF task including entropy (EN) (Roberts, Van Aardt, and Ahmed 2008), standard deviation (SD) (Eskicioglu and Fisher 1995), spatial frequency (SF) (Ma, Ma, and Li 2019), visual information fidelity (VIF) (Han et al. 2013), sum of correlation of differences (SCD) (Ma, Ma, and Li 2019), mutual information (MI) (Ma, Ma, and Li 2019), $Q^{AB/F}$ (Ma, Ma, and Li 2019) and structural similarity index measure (SSIM) (Wang et al. 2004). Tab. 1 and Tab. 2 demonstrate the quantitative comparison results on Harvard MRI-CT, MRI-PET, MRI-SPECT and our *BraTS-Fuse* dataset with two modalities, respectively. More experiment results with three and four modalities on our benchmark are shown in the supplementary material.

Table 3: Ablation comparisons of our method on entire quantitative unsupervised metrics. Bold red indicates the best, bold blue indicates the second best.

Configurations	EN	SD	VIF	SF	MI	SCD	Qabf
w/o Reconstruction Decoder	6.50	40.50	0.75	4.20	1.50	0.85	0.65
FILM+nnUnet	6.60	42.20	0.85	4.30	1.60	0.88	0.68
FILM+nnUnet-P	6.65	41.00	0.80	4.25	1.55	0.86	0.67
w/o \mathcal{L}_{Enc}^{adv} in pre-training stage	6.70	46.00	0.89	4.40	1.70	0.90	0.71
w/o \mathcal{L}_{Enc}^{adv} in cooperative training stage	6.78	45.31	0.83	4.38	1.65	0.89	0.70
w/o cross-attention mechanism	6.73	43.79	0.86	4.35	1.62	0.88	0.69
Ours	6.86	47.05	0.98	4.50	1.75	0.95	0.75

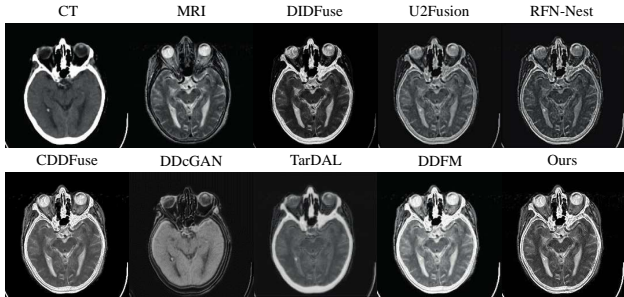


Figure 6: Qualitative comparison results on Harvard dataset.

Results of medical image segmentation

In this section, we test the image segmentation results with the state-of-the-art methods including UNet 3+(Huang et al. 2020), AttnUNet(Oktay et al. 2018), SwinUNet(Cao et al. 2022), CASCADE(Rahman and Marculescu 2023), EM-CAD(Rahman, Munir, and Marculescu 2024). Moreover, we construct additional baseline by combing the state-of-the-art image fusion method, *i.e.*, FILM(Zhao et al. 2024), with segmentation nnUnet(Isensee et al. 2021), which is labeled as **FILM+nnUnet**. To make fair comparison, we further add our pre-trained encoder into this framework and construct a baseline labeled as **FILM+nnUnet-P**. We choose three effective metrics to measure the quantitative performance of MIF task, *i.e.*, DICE score, mIoU and HD95. Tab. 1 demonstrate the quantitative comparison results our *BraTS-Fuse* dataset with two modalities, respectively. More experiment results with three and four modalities on our benchmark are shown in the supplementary material.

Ablation Studies

To evaluate the effectiveness of our proposed architecture, we conducted a comprehensive ablation study. Initially, we eliminated the reconstruction decoder from the fusion network structure and modified the inputs of the segmentation network to directly utilize the fused embedding, rather than the complete fused image. The results of this ablation experiment were particularly illuminating. Our quantitative analysis revealed that this alternative approach yielded inferior performance metrics compared to our original architectural

design, underscoring the critical role of the complete fused image as a conditioning input for the segmentation task. Moreover, to gauge the full potential and limitations of our model, we systematically adjusted the network architecture. This additional set of experiments was designed to determine the upper and lower bounds of the model’s capabilities, enabling us to identify the optimal structural configuration. We evaluate the model in the situation of w/o \mathcal{L}_{Enc}^{adv} in pre-training stage and cooperative training stage, test the model w/o attention module to demonstrate cross-modality ability.

Furthermore, we demonstrated the generalizability of our Fuse4Seg structure by implementing two variants: FILM+nnUnet and FILM+nnUnet-P in Tab. 1 and Tab. 3. Both methods consistently outperformed their vanilla counterparts, underscoring the potential of our Fuse4Seg structure as a general enhancement framework for existing segmentation models. More results shown in supplementary materials.

Conclusion and Extensions

This paper introduces a novel image-level fusion method for multi-modality medical image segmentation. Our approach, for the first time, employs bi-level learning to simultaneously optimize the medical image fusion network and segmentation network (*Fuse4Seg*), utilizing a pre-trained feature decomposition encoder and a cross-modal attention mechanism-guided fusion network, with a skip-connected transformer encoder serving as the segmentation network. This method enhances the accuracy and interpretability of fused images, as demonstrated through rigorous evaluations on the proposed *BraTS-Fusion* benchmark and other public datasets. Our method, originally designed for medical image multimodal fusion, shows promising potential for extension to natural images. To evaluate this, we tested our method on several natural image datasets, including TNO and MSRS, and observed that it maintains its capability to integrate diverse sources of information to produce high-quality fusion results. Future work will focus on expanding our approach to other natural image scenarios, assessing its effectiveness across additional datasets, and refining the method to further enhance its versatility and performance.

Acknowledgement

Our work was supported in part by the Guangdong Provincial Key Laboratory of Interdisciplinary Research and Application for Data Science, BNU-HKBU United International College, project code 2022B1212010006, and in part by Guangdong Higher Education Upgrading Plan (2021-2025) of "Rushing to the Top, Making Up Shortcomings and Strengthening Special Features" with UIC research grant UICR0400006-24.

References

- Ardizzone, L.; Kruse, J.; Wirkert, S.; Rahner, D.; Pellegrini, E. W.; Klessen, R. S.; Maier-Hein, L.; Rother, C.; and Köthe, U. 2018. Analyzing inverse problems with invertible neural networks. *arXiv preprint arXiv:1808.04730*.
- Atrey, K.; Singh, B. K.; and Bodhey, N. K. 2024. Multimodal classification of breast cancer using feature level fusion of mammogram and ultrasound images in machine learning paradigm. *Multimedia Tools and Applications*, 83(7): 21347–21368.
- Cao, H.; Wang, Y.; Chen, J.; Jiang, D.; Zhang, X.; Tian, Q.; and Wang, M. 2022. Swin-unet: Unet-like pure transformer for medical image segmentation. In *European conference on computer vision*, 205–218. Springer.
- Chen, G.; Li, L.; Dai, Y.; Zhang, J.; and Yap, M. H. 2022. AAU-net: an adaptive attention U-net for breast lesions segmentation in ultrasound images. *IEEE Transactions on Medical Imaging*, 42(5): 1289–1300.
- Chen, J.; Lu, Y.; Yu, Q.; Luo, X.; Adeli, E.; Wang, Y.; Lu, L.; Yuille, A. L.; and Zhou, Y. 2021. Transunet: Transformers make strong encoders for medical image segmentation. *arXiv preprint arXiv:2102.04306*.
- Chen, L.-C.; Papandreou, G.; Kokkinos, I.; Murphy, K.; and Yuille, A. L. 2017. Deeplab: Semantic image segmentation with deep convolutional nets, atrous convolution, and fully connected crfs. *IEEE transactions on pattern analysis and machine intelligence*, 40(4): 834–848.
- Chen, L.-C.; Zhu, Y.; Papandreou, G.; Schroff, F.; and Adam, H. 2018. Encoder-decoder with atrous separable convolution for semantic image segmentation. In *Proceedings of the European conference on computer vision (ECCV)*, 801–818.
- Cheng, J.; Ye, J.; Deng, Z.; Chen, J.; Li, T.; Wang, H.; Su, Y.; Huang, Z.; Chen, J.; Jiang, L.; et al. 2023. Sam-med2d. *arXiv preprint arXiv:2308.16184*.
- Colson, B.; Marcotte, P.; and Savard, G. 2007. An overview of bilevel optimization. *Annals of operations research*, 153: 235–256.
- Eskicioglu, A. M.; and Fisher, P. S. 1995. Image quality measures and their performance. *IEEE Transactions on communications*, 43(12): 2959–2965.
- Fan, X.; Wang, X.; Gao, J.; Wang, J.; Luo, Z.; and Liu, R. 2024. Bi-level Learning of Task-Specific Decoders for Joint Registration and One-Shot Medical Image Segmentation. In *Proceedings of the IEEE/CVF Conference on Computer Vision and Pattern Recognition*, 11726–11735.
- Han, Y.; Cai, Y.; Cao, Y.; and Xu, X. 2013. A new image fusion performance metric based on visual information fidelity. *Information fusion*, 14(2): 127–135.
- Huang, H.; Lin, L.; Tong, R.; Hu, H.; Zhang, Q.; Iwamoto, Y.; Han, X.; Chen, Y.-W.; and Wu, J. 2020. Unet 3+: A full-scale connected unet for medical image segmentation. In *ICASSP 2020-2020 IEEE international conference on acoustics, speech and signal processing (ICASSP)*, 1055–1059. IEEE.
- Ibtehaz, N.; and Kihara, D. 2023. Acc-unet: A completely convolutional unet model for the 2020s. In *International Conference on Medical Image Computing and Computer-Assisted Intervention*, 692–702. Springer.
- Isensee, F.; Jaeger, P. F.; Kohl, S. A.; Petersen, J.; and Maier-Hein, K. H. 2021. nnU-Net: a self-configuring method for deep learning-based biomedical image segmentation. *Nature methods*, 18(2): 203–211.
- Isensee, F.; Petersen, J.; Klein, A.; Zimmerer, D.; Jaeger, P. F.; Kohl, S.; Wasserthal, J.; Koehler, G.; Norajitra, T.; Wirkert, S.; et al. 2018. nnu-net: Self-adapting framework for u-net-based medical image segmentation. *arXiv preprint arXiv:1809.10486*.
- Isensee, F.; Schell, M.; Pflueger, I.; Brugnara, G.; Bonekamp, D.; Neuberger, U.; Wick, A.; Schlemmer, H.-P.; Heiland, S.; Wick, W.; et al. 2019. Automated brain extraction of multisequence MRI using artificial neural networks. *Human brain mapping*, 40(17): 4952–4964.
- Li, H.; and Wu, X.-J. 2018. DenseFuse: A fusion approach to infrared and visible images. *IEEE Transactions on Image Processing*, 28(5): 2614–2623.
- Li, H.; Wu, X.-J.; and Kittler, J. 2021a. RFN-Nest: An end-to-end residual fusion network for infrared and visible images. *Information Fusion*, 73: 72–86.
- Li, H.; Wu, X.-J.; and Kittler, J. 2021b. RFN-Nest: An end-to-end residual fusion network for infrared and visible images. *Information Fusion*, 73: 72–86.
- Li, J.; Xia, X.; Li, W.; Li, H.; Wang, X.; Xiao, X.; Wang, R.; Zheng, M.; and Pan, X. 2022. Next-vit: Next generation vision transformer for efficient deployment in realistic industrial scenarios. *arXiv preprint arXiv:2207.05501*.
- Liu, J.; Fan, X.; Huang, Z.; Wu, G.; Liu, R.; Zhong, W.; and Luo, Z. 2022. Target-aware dual adversarial learning and a multi-scenario multi-modality benchmark to fuse infrared and visible for object detection. In *Proceedings of the IEEE/CVF conference on computer vision and pattern recognition*, 5802–5811.
- Liu, J.; Liu, Z.; Wu, G.; Ma, L.; Liu, R.; Zhong, W.; Luo, Z.; and Fan, X. 2023. Multi-interactive feature learning and a full-time multi-modality benchmark for image fusion and segmentation. In *Proceedings of the IEEE/CVF international conference on computer vision*, 8115–8124.
- Lou, A.; Guan, S.; and Loew, M. 2021. DC-UNet: rethinking the U-Net architecture with dual channel efficient CNN for medical image segmentation. In *Medical Imaging 2021: Image Processing*, volume 11596, 758–768. SPIE.

- Lu, J.; Han, J.; Hu, Y.; and Zhang, G. 2016. Multilevel decision-making: A survey. *Information Sciences*, 346: 463–487.
- Ma, J.; Liang, P.; Yu, W.; Chen, C.; Guo, X.; Wu, J.; and Jiang, J. 2020a. Infrared and visible image fusion via detail preserving adversarial learning. *Information Fusion*, 54: 85–98.
- Ma, J.; Ma, Y.; and Li, C. 2019. Infrared and visible image fusion methods and applications: A survey. *Information fusion*, 45: 153–178.
- Ma, J.; Xu, H.; Jiang, J.; Mei, X.; and Zhang, X.-P. 2020b. DDcGAN: A dual-discriminator conditional generative adversarial network for multi-resolution image fusion. *IEEE Transactions on Image Processing*, 29: 4980–4995.
- Ma, J.; Xu, H.; Jiang, J.; Mei, X.; and Zhang, X.-P. 2020c. DDcGAN: A dual-discriminator conditional generative adversarial network for multi-resolution image fusion. *IEEE Transactions on Image Processing*, 29: 4980–4995.
- Ma, J.; Yu, W.; Liang, P.; Li, C.; and Jiang, J. 2019. FusionGAN: A generative adversarial network for infrared and visible image fusion. *Information fusion*, 48: 11–26.
- Ochs, P.; Ranftl, R.; Brox, T.; and Pock, T. 2015. Bilevel optimization with nonsmooth lower level problems. In *Scale Space and Variational Methods in Computer Vision: 5th International Conference, SSVN 2015, Lège-Cap Ferret, France, May 31-June 4, 2015, Proceedings 5*, 654–665. Springer.
- Oktay, O.; Schlemper, J.; Folgoc, L. L.; Lee, M.; Heinrich, M.; Misawa, K.; Mori, K.; McDonagh, S.; Hammerla, N. Y.; Kainz, B.; et al. 2018. Attention u-net: Learning where to look for the pancreas. *arXiv preprint arXiv:1804.03999*.
- Rahman, M. M.; and Marculescu, R. 2023. Medical image segmentation via cascaded attention decoding. In *Proceedings of the IEEE/CVF Winter Conference on Applications of Computer Vision*, 6222–6231.
- Rahman, M. M.; Munir, M.; and Marculescu, R. 2024. Emcad: Efficient multi-scale convolutional attention decoding for medical image segmentation. In *Proceedings of the IEEE/CVF Conference on Computer Vision and Pattern Recognition*, 11769–11779.
- Roberts, J. W.; Van Aardt, J. A.; and Ahmed, F. B. 2008. Assessment of image fusion procedures using entropy, image quality, and multispectral classification. *Journal of Applied Remote Sensing*, 2(1): 023522.
- Si, C.; Yu, W.; Zhou, P.; Zhou, Y.; Wang, X.; and Yan, S. 2022. Inception transformer. *Advances in Neural Information Processing Systems*, 35: 23495–23509.
- Sun, Y.; Cao, B.; Zhu, P.; and Hu, Q. 2022. Dctfusion: A detection-driven infrared and visible image fusion network. In *Proceedings of the 30th ACM international conference on multimedia*, 4003–4011.
- Tang, L.; Yuan, J.; and Ma, J. 2022. Image fusion in the loop of high-level vision tasks: A semantic-aware real-time infrared and visible image fusion network. *Information Fusion*, 82: 28–42.
- Wang, Z.; Bovik, A. C.; Sheikh, H. R.; and Simoncelli, E. P. 2004. Image quality assessment: from error visibility to structural similarity. *IEEE transactions on image processing*, 13(4): 600–612.
- Wu, Z.; Liu, Z.; Lin, J.; Lin, Y.; and Han, S. 2020. Lite transformer with long-short range attention. *arXiv preprint arXiv:2004.11886*.
- Xu, H.; Ma, J.; Jiang, J.; Guo, X.; and Ling, H. 2020. U2Fusion: A unified unsupervised image fusion network. *IEEE Transactions on Pattern Analysis and Machine Intelligence*, 44(1): 502–518.
- Zhang, H.; and Ma, J. 2021. SDNet: A versatile squeeze-and-decomposition network for real-time image fusion. *International Journal of Computer Vision*, 129(10): 2761–2785.
- Zhao, Z.; Bai, H.; Zhang, J.; Zhang, Y.; Xu, S.; Lin, Z.; Timofte, R.; and Van Gool, L. 2023a. Cddfuse: Correlation-driven dual-branch feature decomposition for multi-modality image fusion. In *Proceedings of the IEEE/CVF conference on computer vision and pattern recognition*, 5906–5916.
- Zhao, Z.; Bai, H.; Zhu, Y.; Zhang, J.; Xu, S.; Zhang, Y.; Zhang, K.; Meng, D.; Timofte, R.; and Van Gool, L. 2023b. DDFM: denoising diffusion model for multi-modality image fusion. In *Proceedings of the IEEE/CVF International Conference on Computer Vision*, 8082–8093.
- Zhao, Z.; Bai, H.; Zhu, Y.; Zhang, J.; Xu, S.; Zhang, Y.; Zhang, K.; Meng, D.; Timofte, R.; and Van Gool, L. 2023c. DDFM: denoising diffusion model for multi-modality image fusion. In *Proceedings of the IEEE/CVF International Conference on Computer Vision*, 8082–8093.
- Zhao, Z.; Deng, L.; Bai, H.; Cui, Y.; Zhang, Z.; Zhang, Y.; Qin, H.; Chen, D.; Zhang, J.; Wang, P.; et al. 2024. Image Fusion via Vision-Language Model. *arXiv preprint arXiv:2402.02235*.
- Zhao, Z.; Xu, S.; Zhang, C.; Liu, J.; Li, P.; and Zhang, J. 2020. DIDFuse: Deep image decomposition for infrared and visible image fusion. *arXiv preprint arXiv:2003.09210*.